`

Laser-assisted Control of Internal Flows in Evaporating Sessile Ethanol Droplets

A. V. Dyshlyuk(orcid.org/0000-0001-5804-6579)[a,b]*

[a] *Institute of Automation and Control Processes, Far Eastern Branch of Russian Academy of Sciences (IACP FEB RAS), Vladivostok, 690041 Russia*

[b] *Vladivostok State University (VVSU), Vladivostok, 690041 Russia*

**e-mail: anton_dys@iacp.dvo.ru*

Received
Revised
Accepted

Abstract — The paper studies fluid flows in evaporating sessile ethanol droplets subjected to heating by CW laser radiation via the light-absorbing substrate. The flow dynamics under the combined effect of evaporative cooling and localized laser heating were investigated using a fully coupled nonisothermal flow finite element model incorporating the Arbitrary Lagrangian-Eulerian moving mesh methodology to accurately capture the motion of the droplet surface due to evaporation in the constant contact angle mode. The competition between Marangoni flows driven by these two thermal mechanisms and the resulting control over the flow pattern, average temperature and droplet evaporation time is elucidated. It is shown that flow switching to the laser-induced circulation pattern is characterized by flow velocities more than an order of magnitude faster than the pre-laser state. This flow reorganization significantly increased the droplet's average temperature and drastically reduced the total evaporation time. The findings of the study provide new foundations for active control of droplet dynamics in microfluidic and coating technologies.

Keywords: Thermal Marangoni effect, sessile droplets, laser induced heating, liquid flow, microfluidics, lab-on-chip.

INTRODUCTION

The manipulation of internal flows within liquid droplets has recently emerged as an important research area driven by rapid advancements in microfluidics, high-throughput chemical diagnostics, and the development of sophisticated lab-on-a-chip platforms [1-8]. These miniaturized systems are pivotal for a wide range of applications, including biochemistry, targeted medicine, food science, and the detection of environmental or man-made threats.

A variety of external stimuli have been employed to actuate and control fluid flow, including electric [9], magnetic [10], and acoustic fields [11], as well as bulk thermal gradients [12] and mechanical stress [13]. Among these, optical methods [14], particularly those utilizing laser radiation,

`

stand out as exceptionally promising. The proliferation of advanced, cost-effective laser systems offers unparalleled spatiotemporal and spectral control of energy deposition. Key attributes of laser light—such as high monochromaticity, coherence, spatial directivity, and the ability to be tightly focused—coupled with options for high-intensity continuous-wave (CW) or pulsed operation, provide remarkable flexibility for manipulating fluidic processes in small-scale environments like droplets [15-18].

The Marangoni effect, which describes fluid flow driven by gradients in surface tension (σ) presents a highly efficient mechanism for achieving this optical control [19-20]. This effect manifests in two primary forms: solutal Marangoni flow, arising from concentration gradients in multicomponent solutions, and thermal Marangoni (or thermocapillary) flow, which is present even in single-component liquids and results from the temperature dependence of σ ($d\sigma/dT$). For applications involving laser actuation, the thermal Marangoni effect is particularly advantageous. This is because a precise, localized temperature distribution—the driving force for the flow—can be readily established and dynamically controlled by applying laser energy either directly to the absorbing fluid or, for transparent liquids, to an underlying substrate.

One of the most interesting and important areas of fluid dynamics where laser-assisted control is particularly desired is the evaporation of highly volatile liquid droplets, such as ethanol [21-23]. Rapid evaporation from the droplet surface, which is most pronounced at the three-phase contact line, induces strong evaporative cooling. This non-uniform cooling combined with heat inflow from a massive substrate establishes its own spontaneous thermal gradient across the interface, thereby driving an intrinsic thermocapillary flow even in the absence of external heating.

This spontaneous, cooling-driven flow directly interacts and competes with the classic capillary-driven flow responsible for the ubiquitous "coffee-ring effect"—a major challenge in applications requiring uniform deposition of solutes [24-26]. Therefore, when external laser radiation is applied to manipulate an evaporating droplet, the resulting photothermally-induced Marangoni flow does not occur in a quiescent liquid. Instead, it is actively superimposed upon, and competes or collaborates with, both the intrinsic evaporative (thermocapillary) flow and the capillary flow. Understanding the dynamics of this complex interplay is critical for achieving true control over particle transport and final deposit morphology in systems utilizing volatile solvents.

The objective of the present study is, therefore, to fundamentally investigate the fluid dynamics induced by the thermal Marangoni effect in evaporating volatile liquid droplets when subjected to controlling CW laser radiation. We specifically examine the detailed characteristics of the liquid motion, encompassing both the evaporation-induced flows and the flows due to the targeted laser heating of the droplet. Since ethanol, chosen as a representative highly volatile liquid, is transparent across the visible and most of the near-infrared range, the applied laser light is assumed to be effectively absorbed by the substrate beneath the droplet, which then conveys the heat to the liquid primarily via conduction.

`

METHODOLOGY OF THE STUDY

I. Governing Equations and Simplifications

The fluid flow within the droplet is fundamentally governed by the laws of conservation of mass, momentum, and energy, collectively represented by the Navier-Stokes equations [27, 28]:

1) The Continuity Equation (Conservation of Mass):

$$\frac{\mathrm{d}\rho}{\mathrm{d}t} + \nabla \cdot (\rho \boldsymbol{u}) = 0$$

2) The Momentum Equation (Navier-Stokes Equation, Conservation of Momentum):

$$\rho\left(\frac{\partial \boldsymbol{u}}{\partial t} + (\boldsymbol{u} \cdot \nabla)\boldsymbol{u}\right) = -\nabla p + \nabla \cdot \boldsymbol{K} + \boldsymbol{F}$$

3) The Energy Equation (Conservation of Energy, expressed in terms of temperature T):

$$\rho C_p\left(\frac{\partial T}{\partial t} + (\mathbf{u} \cdot \nabla)T\right) = -\nabla \cdot \boldsymbol{q} + Q + \boldsymbol{K}\!:\boldsymbol{S},$$

where ρ is the density, $\boldsymbol{u}$ is the velocity vector, p is pressure, $\boldsymbol{K}$ is the viscous stress tensor, $\boldsymbol{F}$ is the volume force vector, C_p is the specific heat capacity at constant pressure, $\boldsymbol{q}$ is the heat flux vector, Q represents internal heat sources, and S is the strain-rate tensor.

We model the liquid within the droplet as Newtonian, which establishes the constitutive relation for the viscous stress tensor:

$$K = 2\mu\boldsymbol{S} - \left(\frac{2}{3}\mu - \lambda\right)(\nabla \cdot \boldsymbol{u})\boldsymbol{I},$$

where μ is the dynamic viscosity, λ is the bulk viscosity, and $\boldsymbol{I}$ is the identity matrix.

To simplify the numerical solution under the assumption of moderate-power laser irradiation, we treat the liquid as incompressible and assume constant density ($\rho = \mathrm{const}$). This is justified by the relatively small temperature variations, which renders the Boussinesq approximation unnecessary in this specific context.

Under the incompressible assumption ($\nabla \cdot \boldsymbol{u} = 0$) and utilizing the Newtonian constitutive relation, the governing equations are reduced to the simplified, more manageable form used for computational analysis:

1) Simplified Continuity:

$$\nabla \cdot \boldsymbol{u} = 0$$

2) Simplified Momentum (Incompressible Navier-Stokes):

$$\rho\left(\frac{\partial \boldsymbol{u}}{\partial t} + (\boldsymbol{u} \cdot \nabla)\boldsymbol{u}\right) = -\nabla p + \mu\nabla^2\boldsymbol{u} + \boldsymbol{F}$$

Given the small size of the modeled droplet (contact area radius is R=1mm), the effect of gravity is considered negligible. Consequently, the initial droplet shape (at t=0) is determined solely by the surface tension forces and is assumed to be a spherical segment defined by a specified contact angle, of which we considered three representative values: θ=25^0, 45^0 and 65^0.

The temperature distribution $T(r,t)$ within the droplet—which is the fundamental driver of the thermal Marangoni effect—is computed by solving the energy conservation equation for heat transfer in fluids:

$$\rho C_p\left(\frac{\partial T}{\partial t} + (\boldsymbol{u} \cdot \nabla)T\right) = \nabla \cdot (k\nabla T) + Q$$

`

Where k is the thermal conductivity. This equation simultaneously accounts for transient heating (the $\partial T / \partial t$ term, or thermal storage), heat conduction (the $\nabla \cdot (k\nabla T)$ term, i.e., diffusive heat flux) and heat convection (the $\rho C_p(\boldsymbol{u} \cdot \nabla)T$ term), representing the transport of heat carried by the moving fluid. The term Q represents any volumetric heat sources. In this work, where the laser is assumed to be absorbed by the substrate, Q is set to zero within the fluid. Instead, the heating is applied as a prescribed temperature boundary condition at the liquid-substrate interface.

The thermal model is fully coupled with the Navier-Stokes equations governing the fluid flow as illustrated in Fig. 1a-c. The velocity field $\boldsymbol{u}$, calculated by the Navier-Stokes equations, is fed into the convective term $(\boldsymbol{u} \cdot \nabla)T$ of the heat equation, ensuring that the fluid motion itself redistributes the heat. The resulting temperature field T is used to calculate the temperature-dependent surface tension $\sigma(T)$ at the droplet surface (Fig. 1a,b). The gradient of this tension, ∇_s, is then applied as the primary Marangoni force boundary condition at the free surface, which in turn drives the fluid velocity $\boldsymbol{u}$ (see the left-hand side of Fig. 1c).

<Fig. 1>

For volatile liquids such as ethanol, the evaporative phase transition at the liquid-gas free surface is a critical physical process. This process results in evaporative cooling, a non-uniform heat loss (q_{evap}) that must be applied as a boundary condition to the energy equation at the droplet's free surface:

$$q_{evap} = J(\boldsymbol{r}) \cdot L_v,$$

where, L_v is the latent heat of vaporization, and $J(\boldsymbol{r})$ is the local evaporative mass flux ($\mathrm{kg \cdot m^{-2} \cdot s^{-1}}$) on the surface as shown schematically with black arrows in the right-hand side of Fig. 1c.

In this work, we adopt the widely recognized methodology of Hu and Larson [29] to calculate this flux. This model assumes the evaporation is a quasi-static, diffusion-limited process, where the mass flux is governed by the diffusion of ethanol vapor from the droplet surface into the surrounding ambient air.

The ethanol vapor concentration field (C) in the air is assumed to obey the Laplace equation ($\nabla^2 C = 0$), analogous to an electrostatic potential problem. The boundary conditions are:

1. At the droplet surface: The vapor concentration is fixed at its saturated value, $C_{sat} = p_{sat}(T_s)/(R_g T_s)$.
2. At the substrate: The flux is zero (impermeable wall).
3. In the far-field: The concentration is that of the ethanol-free ambient air, i.e. $C_{amb} = 0$.

Solving this problem shows that the evaporative flux $J(\boldsymbol{r})$ is highly non-uniform. For a spherical cap droplet as assumed in this work, the flux increases towards the contact line and in fact diverges at the very edge of the droplet for all θ<90^0 (as illustrated by the black arrows in Fig. 1c) Hu and Larson provide a well-established approximate analytical expression for the flux $J(r)$ as a function of the radial distance *r* from the droplet center:

$$J(r) = J_0 \left(1 - \frac{r^2}{R^2}\right)^{-\lambda(\theta)},$$

where R is the contact radius of the droplet, J_0 is a reference evaporative flux, $\lambda(\theta)$ is an exponent that depends on the contact angle.

`

This non-uniform flux $J(r)$, which is strongest at the edge ($r \to R$), creates the intrinsic temperature gradient for evaporative cooling. This, in turn, drives a spontaneous thermocapillary flow that competes or collaborates with the flow generated by the external laser heating.

II. Computational Domain and Numerical Method

The flow and heat equations are solved numerically in the time domain using the Finite Element Method (FEM) implemented in Comsol Multiphysics software. We employ a non-uniform mesh of triangular elements for spatial discretization (see the right-hand side of Fig. 1a). To resolve the curved surface of the droplet with contact area radius R=1mm we apply to it additional mesh refinement with a mesh element size of 3 μm, which was found, by the mesh convergence study, to be sufficient to suppress non-physical flows in the droplet due to discretization of the smoothly curved droplet surface with a mesh of first-order, straight-edged triangular elements.

To facilitate the modeling and reduce computational cost, we use effectively a 2D axisymmetric formulation to represent the 3D geometry of the evaporating droplet (Fig. 1d). The results obtained from this simplified 2D treatment of the problem under study are considered indicative of the flow characteristics within a truly three-dimensional droplet, although checking the validity limits of the axisymmetric approximation and a rigorous, fully three-dimensional generalization of the obtained results is reserved for future work.

III. Fluid Flow Boundary Conditions

The computational domain, apart from the symmetry axis, has two boundaries: the free liquid surface and the liquid-substrate interface.

A. Free Liquid Surface

At the free surface, the following conditions are imposed for the Navier-Stokes equations:

1. Kinematic Condition: The velocity of the fluid ($\mathbf{u}_{fluid}$) must match the velocity of the mesh (u_{mesh}) in the direction normal to the interface, accounting for mass flux (M_f) due to evaporation:
$$(\mathbf{u}_{fluid} - \boldsymbol{u}_{\text{mesh}}) \cdot n_i = M_f$$
2. Dynamic (Stress) Condition: The stress balance requires that the viscous and pressure forces are balanced by the force generated by surface tension, F_{st}:
$$(-pI + K) \cdot n_i = F_{\text{st}}$$

The surface tension force, which drives the Marangoni flow, is defined as:
$$F_{\text{st}} = \sigma\kappa n_i + \nabla_s \sigma,$$
where σ is the surface tension coefficient, κ is the mean curvature of the surface, and ∇_s is the surface gradient operator. The term $\nabla_s \sigma$ explicitly represents the force due to the surface tension gradient—the thermal Marangoni effect.

B. Liquid-Substrate Interface

At the interface with the substrate, a Navier slip boundary condition is applied to model the fluid-wall interaction more realistically than a simple 'no-slip' condition.

1. No Penetration (Normal Component): The liquid velocity normal to the wall is set to zero:
$$u \cdot n_{wall} = 0$$
2. Navier Slip (Tangential Component): Instead of imposing a zero tangential velocity (the 'no-slip' condition), the tangential stress ($\mathbf{K}_{\boldsymbol{n}_t}$) is set to be proportional to the tangential velocity (u_{slip}):

`

$$\mathbf{K}_{\boldsymbol{n}_t} = -\frac{\mu}{\beta} u_{\text{slip}}$$

where $u_{slip} = u - (u \cdot n_{wall}) n_{wall}$ is the velocity tangential to the wall, μ is the dynamic viscosity, and β is the slip length. This condition physically represents the fact that the extrapolated tangential velocity would be zero at a distance β outside the wall.

IV. Thermal Boundary Conditions

The temperature field $T(r,t)$, governed by the energy conservation equation, requires specific boundary conditions at the domain interfaces:

A. Liquid-Substrate Interface

We assume the liquid in the droplet to be in good thermal contact with a massive substrate maintained at constant temperature so that the temperature of the liquid adjacent to this interface can be considered fixed to the substrate temperature, which is, prior to laser irradiation, 20^0C.

As the laser is turned on, its radiation is assumed to be effectively absorbed by the substrate. In this work, for maximum clarity of the demonstration of the laser effect on the internal flow patterns in evaporating droplets, we take up the simplest possible approach to the laser action on the substrate: we assume that the laser creates a region of time-invariant axially-symmetric elevated temperature distribution at the center of the droplet's contact area. This distribution of additional temperature at the liquid-substrate interface is assumed to be gaussian mimicking a typical laser beam intensity profile. The laser is considered to be of moderate power to ensure that the liquid temperature is high enough to produce an obvious effect on the fluid flows in the droplet but remains below the boiling point. Based on this we deemed the reasonable amplitude of the imposed additional temperature distribution to be 50^0C, so that the maximum temperature of the substrate at the center of the droplet's contact area is 20^0C+50^0C=70^0C. For the gaussian spot size parameter r_0 we take two representative values: r_0=0.1 mm and r_0=0.25 mm.

B. Liquid-Gas Free Surface

The main thermal condition at the free surface is dominated by evaporative cooling, as detailed above. The net heat flux across the free surface must balance the heat transfer due to conduction and evaporation:

$$n \cdot \left(k_{\text{liquid}} \nabla T\right) = q_{\text{evap}} + q_{\text{conv, rad}},$$

where evaporative heat loss (q_{evap}) is the endothermic heat sink caused by the phase change, calculated using the Hu and Larson methodology as $q_{\text{evap}} = J(r) \cdot L_v$. The characteristic feature of the evaporative heat loss is that, following $J(r)$ dependence, it is nearly uniform at the top part of the droplet's surface but increases near the contact line (as shown with black arrows in Fig. 1c), i.e. evaporation-caused cooling of the droplet is the strongest near its contact line. Convective and Radiative Losses ($q_{\text{conv, rad}}$) is the term accounting for heat exchange via natural convection and thermal radiation between the free surface and the surrounding air, and can be approximated as:

$$q_{\text{conv, rad}} = h_{\text{tot}}(T_{\text{surface}} - T_{\text{ambient}}),$$

where h_{tot} is the total heat transfer coefficient, which is typically very small and will, therefore, be neglected in this work compared to the evaporative term, i.e. we assume:

$$n \cdot \left(k_{\text{liquid}} \nabla T\right) = q_{\text{evap}}$$

`

V. Free Surface Dynamics and Moving Mesh Implementation

To accurately capture the deformation and movement of the droplet's free surface driven by internal flow and evaporative mass loss, the Moving Mesh (ALE, Arbitrary Lagrangian-Eulerian) interface is utilized. This approach allows the computational mesh nodes to follow the movement of the physical boundary, thereby maintaining mesh quality in the immediate vicinity of the interface.

The instantaneous position of the free surface is governed by the kinematic boundary condition, which dictates that the velocity of the mesh ($\boldsymbol{u}_{mesh}$) in the direction normal to the interface must equal the fluid velocity $\boldsymbol{u}$ normal to the interface, plus a term accounting for the mass loss due to evaporation (M_f):

$$(\boldsymbol{u} - \boldsymbol{u}_{\boldsymbol{mesh}}) \cdot n = M_f,$$

where n is the normal vector to the interface and M_f is the evaporative mass flux. This condition ensures that the mesh accurately tracks the recession of the free surface caused by the combined effects of fluid flow and evaporation.

The simulation is performed under the assumption of a moving contact line with a constant contact angle θ=const, effectively ignoring contact line pinning. This choice is based on observations that for moderate evaporation rates on certain substrates, after some pinning, which may occur at initial evaporation stages, the contact line breaks free and recedes while maintaining a constant (receding) contact angle.

To implement this, the contact angle θ (the angle between the free surface tangent and the substrate at the contact point) is constrained to the prescribed value (θ=25^0, 45^0 or 65^0) and the velocity of the contact point on the substrate is calculated by the solver such that the constant angle constraint is satisfied throughout the simulation. This allows the contact radius to decrease over time as the droplet volume diminishes due to evaporation. This implementation requires Comsol's robust mesh deformation algorithms to handle the simultaneous movement and shrinkage of the entire computational domain as the droplet recedes.

RESULTS AND DISCUSSION

Fig.2 presents the results of modelling evaporation of a sessile ethanol droplet with contact angle θ=45^0 and contact area radius R=1mm. To clearly distinguish between flow patterns caused by evaporation and by the applied laser radiation (laser beam gaussian radius r_0=0.1mm), the latter is turned on 10 seconds after the evaporation started (i.e. at t=10s as indicated by the dashed vertical line marked as 'laser on' in the left panel of Fig. 2) to allow enough time for the evaporation-induced flow to firmly establish before starting to heat the substrate beneath the droplet with laser.

The left panel of Fig. 2 shows the temporal dynamics of the total volume of the evaporating droplet without $V_0(t)$ (black curve) and with $V_1(t)$ (red curve) the laser irradiation. Shown in dark blue color is the temporal dependence of the average temperature $T_{avg}(t)$ of the droplet's liquid during evaporation. The colored insets on the right-hand side of Fig. 1 show instantaneous snapshots of temperature and flow velocity distributions within the droplet at different time points over the course of evaporation.

<Fig.2>

The first snapshot (at t=0.1s) corresponds to the very beginning of the evaporation process. As seen from the temperature distribution the droplet has very nearly homogeneous temperature

`

corresponding to the initial condition of T=20^{0}C. However, the effect of the evaporative cooling is already noticeable near the surface of the droplet and causes weak Marangoni flow towards the contact line where evaporation is the strongest and surface tension σ is higher because of a slightly lower temperature.

At *t*=1s, as seen from the next snapshot, a characteristic evaporation-induced flow pattern is developing with some small secondary vortices still present near the top of the droplet. Finaly at *t*=2s this flow pattern is fully established and persists up to the moment of turning on the laser at *t*=10s. It is interesting to note that contrary to what might be expected from the fact that evaporative cooling is the strongest near the edge of the droplet, the coldest area turns out to be at its top, with the resultant Marangoni flow circulating counter-clockwise: from the periphery to the top of the droplet along its surface and from the center to the edge at its bottom. This is explained by the effect of the isothermal substrate, which imposes its fixed temperature to the liquid at the bottom of the droplet. Therefore, the flow pattern established before turning on the laser must be considered a consequence of not only nonuniform evaporative cooling, but its competitive combination with the heat influx to the droplet from the isothermal substrate.

Turning on the laser at *t*=10s creates nonuniform distribution of increased temperature on the substrate bringing about rapid switching of the flow pattern, which occurs in a timespan of less than 1s, as evident from the snapshots at *t*=10, 10.3 and 11s. At t=10s the heating of the liquid by the substrate is already visible at the center of the droplet's bottom but the flow pattern has not had time to change yet. The transition from the old to the new flow pattern can be readily observed at the *t*=10.3s snapshot, while at *t*=11s the new pattern is clearly firmly established and persist up to the complete drying of the droplet, as illustrated by the last shown snapshot at *t*=60s. The characteristic feature of the laser-induced flow pattern is that the liquid heated by the substrate at the center of the droplet's contact area rises to the top of its surface so that it becomes warmer than the periphery. The resulting thermal Marangoni flow directed clock-wise picks up the heated liquid and carries it toward the periphery. As seen from the color legend bars of the flow velocity distributions, the laser-induced circulation is more than an order of magnitude faster than the oppositely directed circulation, which dominated the flow pattern before turning on the laser.

As seen from the left-hand side panel of Fig. 2, the laser irradiation not only switches the flow pattern in the droplet but also increases the overall average temperature of the droplet: from the sharp step-like temperature rise near *t*=10s to the gradual and increasingly fast heating of the droplet throughout its entire evaporation process. The increasing heating rate is explained by shrinking of the evaporating droplet while keeping the spot size of the applied laser irradiation fixed. This means that the heat influx relative to the decreasing volume of the droplet is increasing, i.e. the heating of the shrinking droplet by the same laser-imposed distribution of elevated temperature becomes increasingly effective.

Rising temperature of the droplet increases its evaporation rate as seen by the red curve in Fig.2 representing the reduction of the droplet volume with time with laser irradiation applied at *t*=10s. As one can see, the evaporation rate is increased immediately after the laser is turned on and brings about a significant cut in evaporation time as compared with evaporation without laser heating (black curve).

Turning on the laser and switching of the flow pattern in the droplet do not necessarily have to occur at the same time. To illustrate this, we present in Fig. 3 the dynamics of the evaporation process

`

for the same droplet irradiated by a laser beam with spot size of r_0=0.1mm instead of r_0=0.25mm as was used in the previous case.

As seen from the presented snapshots of temperature and flow velocity distributions, turning on the laser in this case does not bring about instantaneous switching of the flow pattern up until the moment of about t=77.5s, when the switching does occur, after which the laser-induced flow pattern persists till the final stages of evaporation. Neither the turn-on of the laser leads to major heating and increased evaporation rate of the droplet, apart from the small step-like increase in average temperature due to the local heating of the liquid near the hot spot at the center of droplet's contact area. A much larger step-like rise in temperature accompanies the switching of the flow pattern at t=77.5s, after which laser-induced speeding-up of evaporation becomes obvious from comparing the red and black curves in the left panel of Fig. 3. A sharp rise in average temperature at the flow switching time and its subsequent rapid growth afterwards can be explained by a more efficient heat removal from the heated spot on the substrate by the much faster circulation of liquid after the flow switching.

<Fig.3>

Let us next demonstrate the effect of the droplet contact angle on the dynamics of the laser-assisted evaporation. Fig. 4 below illustrates the details of the evaporation process of a droplet with a contact angle of $\theta=65^0$ and the same contact area radius R=1mm, subjected to laser heating (r_0=0.25mm) at t=10s.

<Fig.4>

From examination of the figure one can conclude that the evaporation process in this case proceeds analogously to that shown in Fig. 2, although it takes somewhat longer time due to a larger initial volume of the droplet. The flow pattern induced by the combined effect of evaporative cooling and heat influx through the isothermal substrate (before turning on the laser) and the flow pattern imposed by the laser irradiation (after flow switching) are very similar to those observed in the previously studied case, with the liquid circulating, respectively, counter-clockwise and clockwise. The flow switching occurs right after turning on the laser, but this time with a short but noticeable delay of about 3s.

This delay also increases, as compared with the previously studied case, when the laser beam radius is r_0=0.1mm as illustrated in Fig.5.

<Fig.5>

As seen from the figure, it takes almost 140s for the flows to switch to the laser-induced pattern after turning on the laser, so that most of the evaporation process proceeds virtually unaffected by the laser irradiation in terms of the flow pattern, evaporation rate and average temperature dynamics. The flow patterns before and after switching are again very similar to those in the previously studied cases.

Finally, let us examine the case of laser-assisted evaporation of a droplet with a small contact angle of $\theta=25^0$, R=1mm, r_0=0.1mm (Fig. 6).

<Fig.6>

The distinctive feature of the evaporation process in this case is that no equilibrium flow pattern is reached before turning on the laser, as evidenced by the small ripples in the average temperature curve before t=10s in the left panel of Fig. 6. This is illustrated in more detail by the snapshots of temperature and flow velocity distributions at t=1s, 2s and 3s on the right-hand side of the figure. As

`

evident from the snapshots, the flow distribution continuously cycles back and forth between the 2- and 3-vortex patterns. This is a result of competition between the nonuniform evaporative cooling, which strives to set up Marangoni flow from the top of the droplet surface towards the contact line, and the effect of the isothermal substrate, which, by heating the droplet from below, tries to impose the oppositely directed Marangoni flow.

Turning on the laser at t=10s instantaneously disrupts this delicate interplay and the flows adopt at once the pattern characteristic of the laser-assisted evaporation, as shown above. This pattern then persists to the final stages of evaporation, which takes, in this case, as little as 50s due to the small initial volume of the droplet.

CONCLUSIONS

Thus, in this work we have numerically investigated the temporal dynamics of fluid flows in sessile ethanol droplets evaporating in the constant contact angle mode both without and with laser irradiation, which heats the transparent droplet via light-absorbing substrate. The investigation elucidated the complex thermal-capillary interplay governing the internal fluid dynamics and droplet lifetime, demonstrating the potential for precise external control. It was shown that before laser activation, the flow pattern is dictated by a competitive thermal balance: nonuniform evaporative cooling at the free surface strives to induce thermal Marangoni flow toward the contact line, where the cooling is the strongest. On the other hand, the heat influx from the isothermal substrate attempts to impose the opposite Marangoni flow by fixing the liquid temperature at the droplet bottom to that of the substrate. This initial competition results in a stable flow pattern, characterized by the coldest point at the droplet's apex and a counter-clockwise liquid circulation (periphery to center along the surface), although this balance is shown to be unstable for small contact angles $\theta=25^0$, leading to continuous oscillation between 2- and 3-vortex patterns. Activating the laser at t=10s instantaneously disrupts this delicate balance, causing the flow pattern to rapidly switch to the laser-induced pattern. This new regime is characterized by a strong clockwise circulating flow (center to periphery) driven by the substrate-heated liquid rising at the droplet center. This laser-induced circulation is significantly faster (more than an order of magnitude) than the native evaporation-driven flow. Crucially, this robust flow pattern facilitates a more efficient heat removal from the heated area, leading to a marked increase in the droplet's average temperature and a significant reduction in the total evaporation time. The study also revealed that the time required for this decisive flow switching is highly dependent on both the laser spot size and the contact angle. While a larger laser spot (r_0=0.25mm) causes switching to be near-instantaneous (less than a few seconds), a smaller spot (r_0=0.1mm) can introduce a substantial delay (up to ~140s for $\theta=65^0$), during which the evaporation process remains virtually unaffected by the applied laser irradiation.

The results obtained in the chemical analysis and medical diagnostics - for rapid mixing of liquid in multicomponent droplets, for the implementation of laser-controlled movement of droplets on superhydrophobic substrates, including lab-on-chip systems. The demonstrated effects can also be used as an additional mechanism for controlling liquid flows in evaporating droplets in order to tailor the distribution of impurity deposits on the substrate after total drying of the droplet.

The demonstrated ability to precisely and dynamically switch internal fluid flow pattern via controlled laser irradiation can find practical application in advanced active flow control. The findings

`

of the study enable one to optimize new microfluidic systems for heat management and droplet transport, and are particularly relevant to inkjet printing, material synthesis, fabricating functional materials on surfaces, and developing lab-on-a-chip devices.

FUNDING

The presented study is performed within the state task of IACP FEB RAS (121021600267-6, FWFW-2021-0001).

CONFLICT OF INTEREST

The author declares that he has no conflicts of interest.

`

REFERENCES

1. Yang C. et al., *Advances in Colloid and Interface Science,* 2022, vol. 306, p. 102724.
2. Yang, Y., Jiang, P., Li, H., Li, W., Li, D., Yan, X., ... & Liao, Q., *The Journal of Physical Chemistry Letters*, 2024, vol. 15, no. 34, p. 8877.
3. Dak, P., Ebrahimi, A., Swaminathan, V., Duarte-Guevara, C., Bashir, R., & Alam, M. A., *Biosensors*, 2016, vol. *6,* no. 2, p.14.
4. Leman, M., Abouakil, F., Griffiths, A. D., & Tabeling, P., *Lab on a Chip*, 2015, vol. 15, no. 3, p. 753.
5. Han, K., Wang, Z., Han, X., Wang, X., Guo, P., Che, P., ... & Jiang, L., *Advanced Functional Materials*, 2022, vol. 32, no. 45, p. 2207738.
6. Pavliuk, G. P., Zhizhchenko, A. Y., Vitrik, O. B., *Bulletin of the Russian Academy of Sciences: Physics*, 2023, vol. 87, no. 3, p 429.
7. Lesev, V. N., Sozaev, V. A., *Bulletin of the Russian Academy of Sciences: Physics*, 2016, vol. 80, p. 689.
8. Inogamov, N. A., Zhakhovsky, V. V., & Khokhlov, V. A., *JETP Letters*, 2022, vol. *115,* no. 1, p. 16.
9. Li, Y., Li, J., Liu, L., Yan, Y., Zhang, Q., Zhang, N., ... & Jiang, L., *Advanced Science*, 2020, vol. *7, no.* 18, p. 2000772.
10. Kim, D., & Lee, J. B. *Journal of the Korean Physical Society*, 2015, vol. *66*, p. 282.
11. Naka, M., Hasegawa, K., *Physics of Fluids*, 2020, vol. *32,* no. 12.
12. Mitsunobu, M., Kobayashi, S., Takeyasu, N., & Kaneta, T. *Analytical Sciences*, 2017, vol. *33,* no 6, p. 709.
13. Jiao, Y., Zhang, Y., Lv, X., Ji, J., Wang, Z., Su, Y., ... & Liu, K. *Langmuir*, vol. *37, no.* 6, p. 2140.
14. Lorenz, R. M., Edgar, J. S., Jeffries, G. D., & Chiu, D. T. *Analytical chemistry*, 2006, vol. *78,* no. 18, p. 6433.
15. He, X., Elmer, J. W., & DebRoy, T. *Journal of applied physics*, 2005, vol. 97*,* no 8.
16. Rivière, D., Selva, B., Chraibi, H., Delabre, U., & Delville, J. P. *Physical Review E*, 2016, vol. *93, no.* 2, p. 023112.
17. Delville, J. P., de Saint Vincent, M. R., Schroll, R. D., Chraibi, H., Issenmann, B., Wunenburger, R., ... & Brasselet, E., *Journal of Optics A: Pure and Applied Optics*, 2009, vol. *11, no.* 3, p. 034015.
18. Wang, Y., Zhang, Q., Zhu, Z., Lin, F., Deng, J., Ku, G., ... & Bao, J., *Science advances*, 2017, vol. *3, no.* 9, p.1700555.
19. Velarde, M. G., & Zeytounian, R. K. (Eds.). *Interfacial phenomena and the Marangoni effect, v*ol. 428, Vienna/New York, Springer, 2002.
20. Hu, H., & Larson, R. G. *The Journal of Physical Chemistry B*, 2006, vol. *110, no.* 14, p. 7090.
21. Chen, C.T., Tseng, F.G. and Chieng, C.C., *Sensors and Actuators A: Physical*, 2006, vol. *130*, pp.12-19.
22. Sodtke, Christof, Vladimir S. Ajaev, and Peter Stephan *Journal of Fluid Mechanics,* 2008 *vol.* 610, pp. 343-362.
23. Maatar, A., et al. *International Journal of Heat and Mass Transfer*, 2015, vol. 86, pp. 212-220.

`

24. Mampallil, Dileep, and Huseyin Burak Eral. *Advances in colloid and interface science,* 2018, vol. 252, pp. 38-54.
25. Yunker, Peter J., et al. *Nature*, 2011, vol. 476.7360, pp. 308-311.
26. Anyfantakis, Manos, and Damien Baigl. *ChemPhysChem*, 2015, 16.13, pp. 2726-2734.
27. R.L. Panton, *Incompressible Flow*, 2nd ed., John Wiley & Sons, 1996.
28. R.B. Bird, W.E. Stewart, and E.N. Lightfoot, *Transport Phenomena*, 2nd ed., John Wiley & Sons, 2007.
29. Hu, Hua, and Ronald G. Larson. *The Journal of Physical Chemistry B*, 2002, 106.6, pp. 1334-1344.

`

FIGURE CAPTIONS

Fig. 1. The ethanol droplet being modelled: (a) – distributions of temperature and resulting surface tension on the droplet surface as functions of the radial distance r in the plane of liquid-substrate interface; (b) – temperature dependence of ethanol's surface tension used to calculate $\sigma(r)$ in (a); (c) – side view of the axisymmetric ethanol droplet being modelled. Shown on the left half is the temperature and flow velocity distribution for the steady-state flow pattern induced by the combined effect of nonuniform evaporative cooling and heat influx through the isothermal substrate, which typically preceded the activation of laser irradiation in our modelling. The big blue arrow indicates the direction of the thermal Marangoni stress driving the flow, which results from the gradient of surface tension shown in (a). On the right half we show the nonuniform mesh of triangular elements that was used for the numerical solution of the Navier-Stokes and heat equation. The mesh is refined at the free surface of the droplet to suppress nonphysical flows. Black arrows indicate the magnitude and direction of the nonuniform evaporative mass flux at the droplet surface; (d) – 3D representation of the axisymmetric sessile ethanol droplet being modelled.

Fig. 2. Temporal evolution of the droplet volume over the course of evaporation without ($V_0(t)$) and with ($V_1(t)$) laser irradiation activated at t=10s. The blue curve shows the average liquid temperature evolution corresponding to $V_1(t)$. Vertical dashed lines indicate the moments of laser heating activation and flow pattern switching. Shown on the right are the snapshots of instantaneous temperature and flow velocity distributions within the droplet at different time points during evaporation. The parameters of the droplet and irradiating laser beam are: R=1mm, $\theta=45^0$, r_0=0.25mm.

Fig. 3. Temporal evolution of the droplet volume and average temperature over the course of evaporation. Shown on the right are the snapshots of instantaneous temperature and flow velocity distributions within the droplet at different time points during evaporation. The parameters of the droplet and irradiating laser beam are: R=1mm, $\theta=45^0$, r_0=0.1mm.

Fig. 4. Temporal evolution of the droplet volume and average temperature over the course of evaporation. Shown on the right are the snapshots of instantaneous temperature and flow velocity distributions within the droplet at different time points during evaporation. The parameters of the droplet and irradiating laser beam are: R=1mm, $\theta=65^0$, r_0=0.25mm.

Fig. 5. Temporal evolution of the droplet volume and average temperature over the course of evaporation. Shown on the right are the snapshots of instantaneous temperature and flow velocity distributions within the droplet at different time points during evaporation. The parameters of the droplet and irradiating laser beam are: R=1mm, $\theta=65^0$, r_0=0.1mm.

Fig. 6. Temporal evolution of the droplet volume and average temperature over the course of evaporation. Shown on the right are the snapshots of instantaneous temperature and flow velocity distributions within the droplet at different time points during evaporation. The parameters of the droplet and irradiating laser beam are: R=1mm, $\theta=25^0$, r_0=0.1mm.

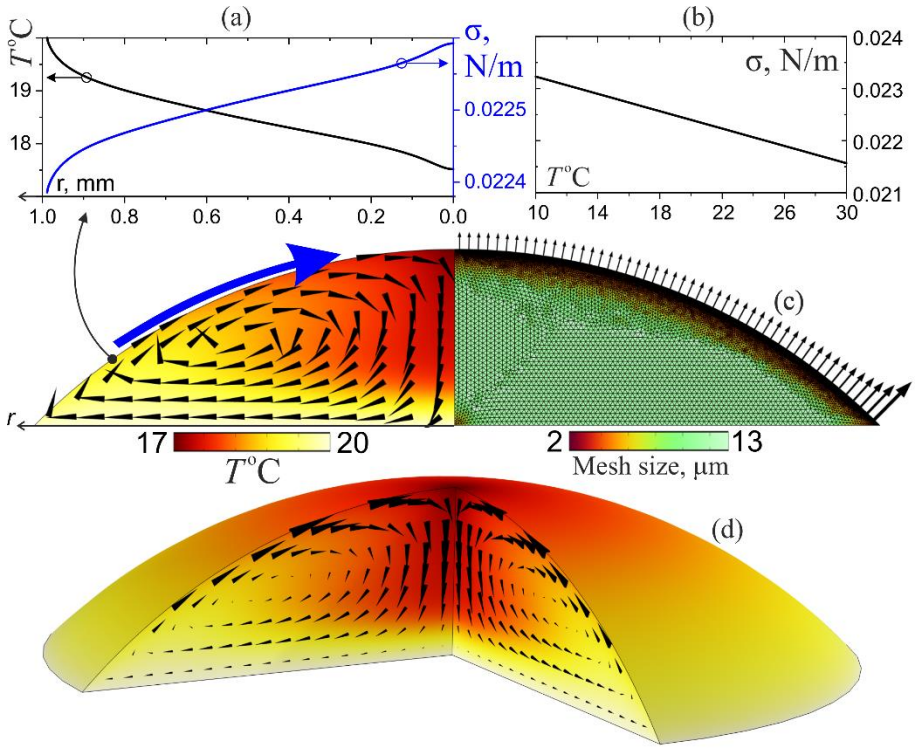
(a)
(b)
(c)
(d)
T°C
σ, N/m
r, mm
17
20
T°C
2
13
Mesh size, μm

Fig. 1.

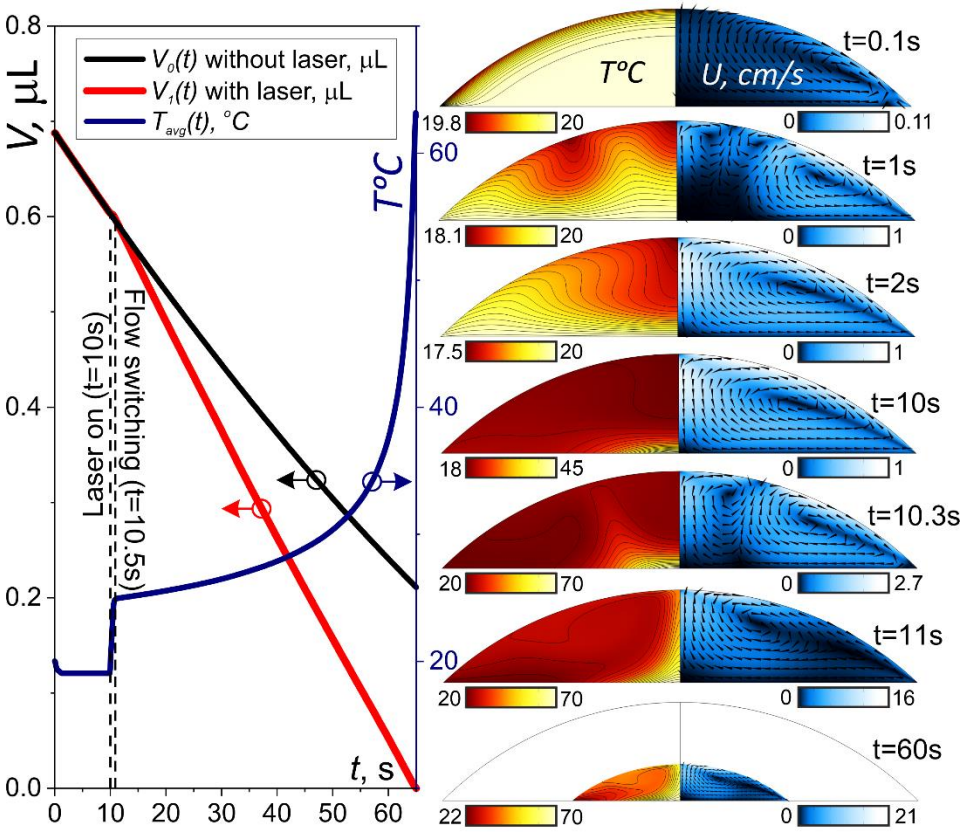
V, μL
$V_0(t)$ without laser, μL
$V_1(t)$ with laser, μL
$T_{avg}(t)$, °C
T°C
Laser on (t=10s)
Flow switching (t=10.5s)
t, s
U, cm/s
t=0.1s
t=1s
t=2s
t=10s
t=10.3s
t=11s
t=60s

Fig. 2.

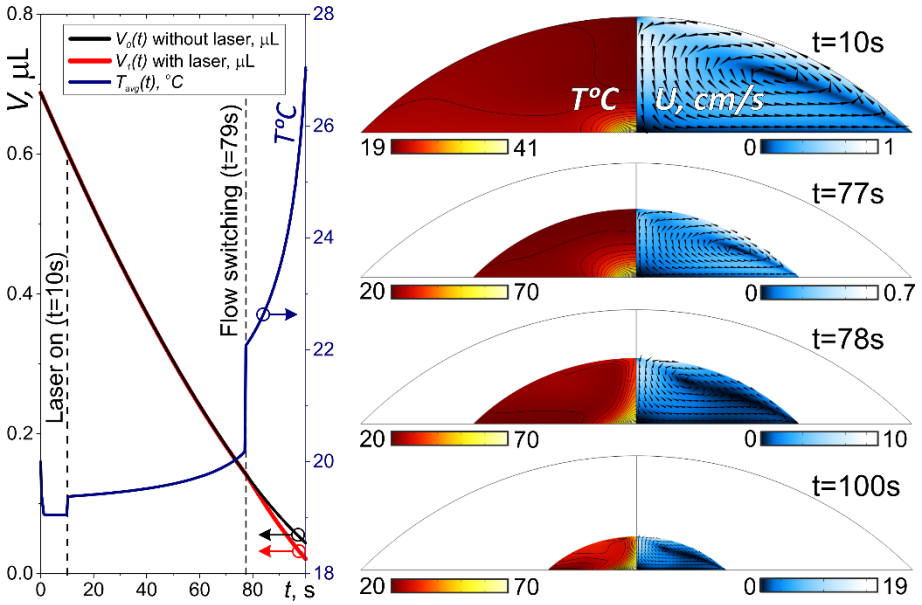
$V_0(t)$ without laser, μL
$V_1(t)$ with laser, μL
$T_{avg}(t)$, °C
V, μL
T°C
t, s
Laser on (t=10s)
Flow switching (t=79s)
t=10s
t=77s
t=78s
t=100s
T°C
U, cm/s

Fig. 3.

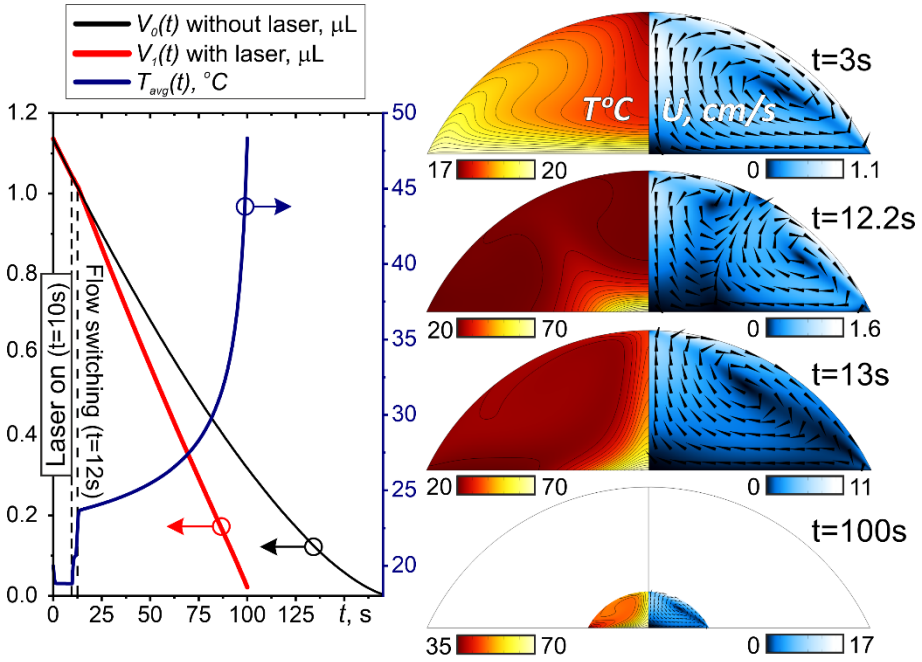
$V_0(t)$ without laser, μL
$V_1(t)$ with laser, μL
$T_{avg}(t)$, °C
t, s
Laser on (t=10s)
Flow switching (t=12s)
t=3s
t=12.2s
t=13s
t=100s
T°C
U, cm/s

Fig. 4.

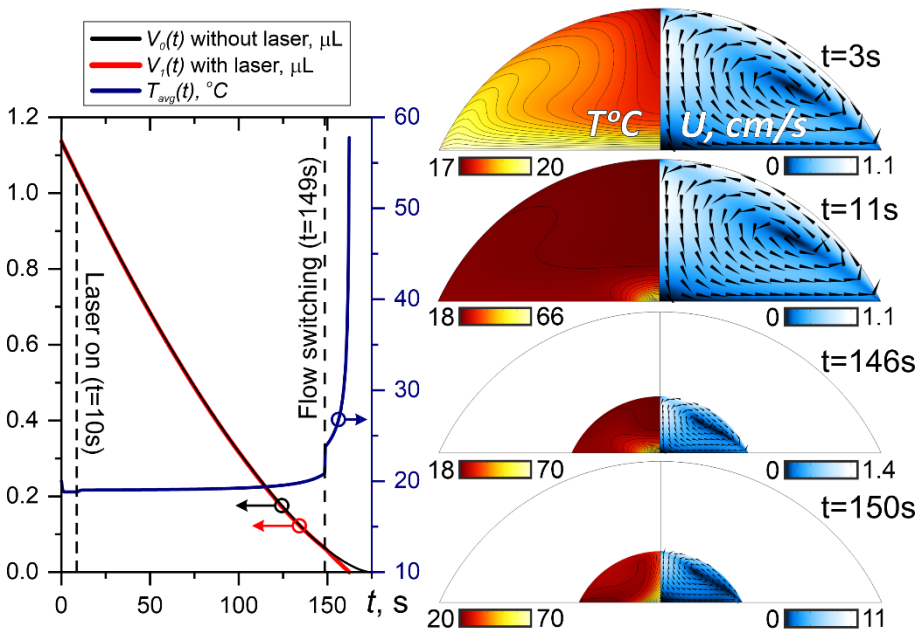
$V_0(t)$ without laser, μL
$V_1(t)$ with laser, μL
$T_{avg}(t)$, °C
Laser on (t=10s)
Flow switching (t=149s)
t, s
T°C
U, cm/s
t=3s
t=11s
t=146s
t=150s

Fig. 5.

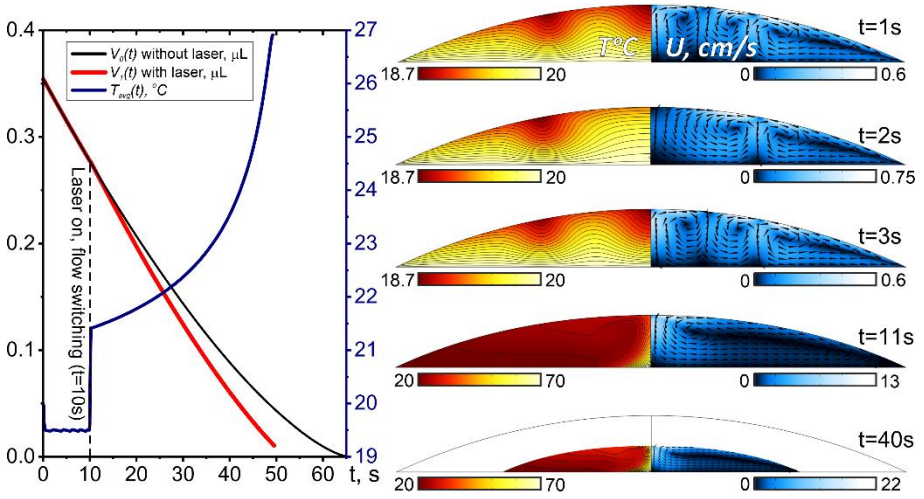
$V_0(t)$ without laser, μL
$V_1(t)$ with laser, μL
$T_{avg}(t)$, °C
Laser on, flow switching (t=10s)
t, s
T°C
U, cm/s
t=1s
t=2s
t=3s
t=11s
t=40s

Fig. 6.